

3D Printed TiO₂ Negative Electrodes for Sodium-Ion and Lithium-Ion Batteries using Vat Photopolymerization

Alexis Maurel^{1,2,}, Ana C. Martinez^{1,2}, Sina Bakhtar Chavari³, Bharat Yelamanchi³, Myeong-Lok Seol⁴, Donald A. Dornbusch⁵, William H. Huddleston⁵, Sreeprasad T. Sreenivasan², Cameroun G. Sherrard⁶, Eric MacDonald¹ and Pedro Cortes^{3,*}*

¹ Department of Aerospace and Mechanical Engineering, The University of Texas at El Paso, El Paso, TX 79968, USA

² Department of Chemistry and Biochemistry, The University of Texas at El Paso, El Paso, TX 79968, USA

³ Materials Science and Engineering Department, Youngstown State University, Youngstown, OH 44555, USA

⁴ NASA Ames Research Center, Universities Space Research Association, Moffett Field, CA 94035, USA

⁵ NASA Glenn Research Center, Cleveland, OH 44135, USA

⁶ NASA Marshall Space Flight Center, Huntsville, AL 35812, USA

KEYWORDS: sodium-ion battery, lithium-ion battery, negative electrode, additive manufacturing, 3D printing

ABSTRACT

Additive manufacturing, also called 3D printing, represents a unique approach to develop three-dimensional shape-conformable batteries with enhanced electrodes, specific surface area, improved ion diffusion, and power. For the first time, the formulation of a composite photocurable resin loaded with battery electrochemically active components was designed to feed a vat photopolymerization (VPP) 3D printer. In direct alignment with NASA's Artemis mission goals to develop sustainable lunar energy storage infrastructure necessary to support long-term human operations, TiO_2 was here selected as an active material for the negative electrode for sodium-ion and lithium-ion batteries due to its abundance on the lunar surface. The TiO_2 loading in the composite photocurable resin and in the resulting VPP-printed negative electrode was increased as high as possible to enhance the electrochemical performance, while simultaneously ensuring the printability and acceptable mechanical strength for sample handling. The effect of thermal post-processing on the electrical, electrochemical and mechanical performance is reported. Finally, a configurational study is implemented to identify the impact of two different electrode designs (cubic and gyroid lattice unit cells) on the electrochemical performance. This work addresses the difficulties related to the introduction of solid particles within a VPP photocurable resin and the need for a compromise between the electrochemical performances and printability to obtain fully functional VPP-printed electrodes.

1. INTRODUCTION

As part of NASA's Artemis program, astronauts will return to the Moon after almost fifty years of anticipation since the last Apollo mission. As part of this new initiative, the development of an Artemis Base Camp, including a lunar terrain vehicle, a habitable mobility platform, a lunar foundation habitation module, along with power generation and energy storage, is expected to be available by the end of 2030. To support longer expeditions on the Moon and to reduce the astronauts' dependence on a terrestrial supply chain, the utilization of local resources available on the Moon, also known as in-situ resource utilization (ISRU), is crucial to develop a sustainable infrastructure. ISRU-derived materials will result in reduction of mass required to be launched from Earth - avoiding the need to send cost-prohibitive payloads on numerous flights. As reported in our recent study¹, versatile and modular additive manufacturing (AM) technologies (also called 3D printing) combined with the use of ISRU materials as 3D print feedstock is expected to significantly assist astronauts during early missions to build a lunar base camp, and manufacture a wide variety of tools including tailored batteries in small quantities.

In this context, titanium dioxide (TiO_2) has been identified as a plausible option for the negative electrode active material due to its abundance on the Moon surface. TiO_2 has several electrochemically-active phases (rutile, anatase, TiO_2 -Bronze, brookite, hollandite, and amorphous) that have been tested for both sodium and lithium-ion batteries^{2,3}. For lithium-ion batteries, the TiO_2 -Bronze phase has shown a pseudocapacitive diffusion process that favors lithium mobility, which results in fast charge-discharge capability, contrary to the solid-state diffusion process observed in other phases^{4,5}. For sodium-ion batteries, both TiO_2 rutile⁶⁻⁸ and anatase⁹⁻¹² have been reported to achieve great sodium storage capabilities, due to the stacking of

distorted edge-sharing TiO_6 octahedra that form tunnels for possible interstitial sites for Na-ion accommodation and suitable sized pathways for Na^+ diffusion ¹².

It has been demonstrated that TiO_2 provides a superior safety and rate capability compared with conventional negative electrodes, graphite and hard carbon, although its high operational voltage lowers the overall energy density of the battery ³. A strategy to increase the latter, as well as the power density, is the creation of three-dimensional (3D) electrode structures that increase the active exchange surface area and enhance the ionic diffusion ¹³. Our team has shown that intricate 3D structures of electrodes, current collector and even a polymer electrolyte can be created via different additive manufacturing processes ^{14–20}. Moreover, AM provides the advantage of creating shape-conformable structures otherwise nonviable through the traditional tape casting method for electrode manufacturing ^{21,22}. Among the different AM options, vat photopolymerization (VPP), using a UV-photocurable resin as material feedstock and a UV laser or projector to selectively manufacture the desired object layer after layer, is of particular interest for the preparation of electrode materials due to the high resolution that can be achieved ²³.

In this work, the development of a TiO_2 -loaded composite photocurable resin for VPP 3D printing of sodium-ion and lithium-ion battery negative electrodes is demonstrated. During the formulation process, the TiO_2 active material loading in the composite photocurable resin was increased as high as possible to enhance the electrochemical performances of the printed electrode. The detrimental effects of the high loading of fillers on the printability aspect were explored. Through the formulation process, the impact of an additional thermal post-processing step on the electrochemical performance was investigated. A configurational study was also performed to identify the impact of various designs (cubic and gyroid) on the electrical, electrochemical and mechanical performances of the electrode. To have a better understanding of the Li^+ diffusion

within the gyroid electrode upon cycling, a simulation study was accomplished. Characterization of the 3D printed composite electrodes is described before and after the thermal post-processing stage. Thermal (thermogravimetric analysis, TGA), mechanical (hardness and flexural test), morphological (scanning electron microscopy, SEM), as well as electrical and electrochemical analysis of the composite negative electrodes are discussed.

2. EXPERIMENTAL SECTION

2.1. Composite photocurable resin formulation.

Employed here as the active material for the negative electrode, the anatase TiO_2 (99.7% trace metals basis, Sigma Aldrich, USA) was thoroughly mixed in a mortar with conductive carbon black Timcal Super C45 ($\text{BET} = 45 \text{ m}^2 \cdot \text{g}^{-1}$ and 20 nm particle size, MSE Supplies) in a 12:1 weight ratio to improve the electronic conductivity. TiO_2/C powder was then mixed with a photopolymer base resin Genesis standard® (Tethon3D, USA) in ratios $\text{TiO}_2:\text{C}:\text{resin}$ 18:1.5:80.5 wt.%. The mixed composite photocurable resin was bottled inside a UV-blocking container and placed on a roller in ambient conditions for at least 24 hours to ensure homogeneity.

2.2. 3D Printing.

Three dimensional computer aided design (CAD) models were designed with nTopology software (nTopology, USA) and an over exposure compensation was performed using Netfabb (Autodesk, USA). The green architectures consist of discs (12.1 mm diameter and 1.09 mm thick) as well as rectangular coupons (ASTM C1161, type B) with solid, cubic and gyroid patterns. Preliminary printing tests of solid electrode discs (100% infill) were performed with a Prusa SL1S masked stereolithography (SLA) printer (Prusa Research, Czech Republic) equipped with a 200 cm^3 capacity tank to store the photocurable resin and a 405 nm UV LED display. The Standard Tessellation Language (stl file) was sliced beforehand into 50 μm thick 2D-slices using PrusaSlicer

software (Prusa Research, Czech Republic), and an initial light exposure time of 85 seconds was set for the 10 first printed layers. Subsequent layers were subjected to light exposure for 55 seconds. A waiting time of 30 seconds between each layer was implemented. To ensure high dimensional resolution of the parts, all electrode designs were prepared using an Admaflex 130 digital light processing (DLP) 3D printer (Admatec, Netherlands). The printer is equipped with a full high definition 405nm UV light projector, and a conveyor foil system ensuring continuous supply of a thin and even layers of the composite resin for each printed layer. The stl files were sliced directly by the printer software into a collection of 10 μm thick 2D-slices. A volume of at least 20 mL of the composite resin was loaded in the printer. An initial light exposure time of 8 seconds was set for the ten first printed layers. Subsequent layers were subjected to an exposure time of 5 seconds. A delay before and after exposure of 1 second was implemented to ensure the removal of air pockets and the complete curing respectively. All the 1920 x 1080 pixels of the individual slice were illuminated. Prior to printing, the bed platform and feedstock system were thoroughly cleaned with isopropyl alcohol to prevent cross contamination.

2.3. Thermal post-processing.

3D printed samples were placed in an alumina boat and introduced inside a GSL tubular furnace (MTI Corporation, USA) for thermal post-processing. A debinding step was initially incorporated to remove the polymer matrix. It first consisted of a heating ramp at a rate of 1 $^{\circ}\text{C}.\text{min}^{-1}$ from room temperature to 150 $^{\circ}\text{C}$, with a second heating ramp at 0.2 $^{\circ}\text{C}.\text{min}^{-1}$ up to 320 $^{\circ}\text{C}$ and a dwelling time of 4h, followed by a third heating ramp at the same rate of 0.2 $^{\circ}\text{C}.\text{min}^{-1}$ up to 400 $^{\circ}\text{C}$ and a dwelling time of 10h. The sintering step consisted of a first heating ramp at 0.2 $^{\circ}\text{C}.\text{min}^{-1}$ between 400 and 500 $^{\circ}\text{C}$, followed by a second heating ramp at 1 $^{\circ}\text{C}.\text{min}^{-1}$ up to 700 $^{\circ}\text{C}$ and a dwelling time of 4h.

Finally, samples were cooled down to room temperature at a rate of 1 °C.min⁻¹. Both steps were performed under an argon flow at 80 mL.min⁻¹.

2.4. Materials characterization.

Thermogravimetric analysis (TGA) was executed by means of a Q50 (TA instrument, USA). Between 3 and 6 mg of material were placed on a Pt pan and analyzed from 25 to 1000 °C at a heating rate of 10 K.min⁻¹, with oxygen or inert gas at 45.0 mL.min⁻¹.

X-ray powder diffraction (XRD) data were acquired with an Empyrean-2 X-ray diffractometer (Malvern Panalytical, UK) using Cu K α radiation ($\lambda = 1.5418 \text{ \AA}$), 45 kV of accelerating voltage, and a current of 40 mA. Data were recorded from 20 to 100° 2theta with a step size of 0.013° and a scan rate of 8°/min.

Material dispersion, sample homogeneity and porosity on the 3D printed and sintered samples were investigated by means of a S-4800 (Hitachi, Japan) field emission scanning electron microscope (SEM) operating in high vacuum mode. Secondary images were recorded with a 15 kV acceleration voltage.

Green state and sintered 3D printed electrodes were placed between two copper plates to measure their resistance across the thickness with a multimeter. Experiments were performed at room temperature. Conductivities were calculated from the Eq. 1, where t is the sample thickness, A is the sample cross sectional area, and R is the resistance.

$$\sigma = \frac{1}{R} \times \frac{t}{A} \quad [1]$$

2.5. Mechanical characterization.

Three point bend tests were conducted on the 3D printed electrodes in both green and sintered states. Dimensions of the coupons subjected to the thermal sintering step were scaled up to take into account the shrinkage. The test specimens were designed and tested based on the ASTM C1161. The tests were conducted on an Universal Instron system with a 100 N load cell. The flexural strength was calculated using Eq. 2, where P is the break force, L the outer (support) span, b the specimen width, and d the specimen thickness.

$$S = \frac{3}{2} \frac{PL}{bd^2} \quad [2]$$

A Nanovea M1 Hardness tester was used to carry out the microhardness testing.²⁴ The instrument used the ASTM E2546 standard as default to calculate the superficial hardness and elastic modulus.

2.6. Electrochemical characterization.

Coin cells were assembled inside an argon-filled glovebox ($\text{H}_2\text{O} < 0.1$ ppm, $\text{O}_2 < 0.1$ ppm) to perform galvanostatic cycling in half-cell configuration. The green state or sintered 3D printed negative electrode samples were used as working electrodes, and sodium metal (ingot, 99.95% purity, Sigma Aldrich, USA) or lithium metal (0.38 mm thick ribbon, 99.9% purity, Sigma Aldrich, USA) was used as the counter and reference electrode. A fiberglass separator (Whatman GE Healthcare) was impregnated with 150 μL of liquid electrolyte consisting of 1M NaPF_6 (98% purity, Sigma Aldrich) in 1:1 wt. ethylene carbonate and propylene carbonate (>99% purity, Sigma Aldrich) with 3wt.% of fluoroethylene carbonate additive (>98% purity, Tokyo Chemical Industry) when tested in sodium-ion configuration, or 1M LiPF_6 in ethylene carbonate and dimethyl carbonate (EC:DMC 1:1 volume ratio) (LP30 liquid electrolyte, Sigma Aldrich) when tested in lithium-ion configuration. Prior cycling, the cells rested for 20h to ensure sufficient electrolyte impregnation. Cells were galvanostatically charged and discharged either at 1 mA.g^{-1} , 5 mA.g^{-1} , and 10 mA.g^{-1} in a potential window of 0.05 - 2.5 V vs. Na/Na^+ or vs. Li/Li^+ . Tests were performed at 25 °C by means of a LBT galvanostat (Arbin Instruments, USA).

3. RESULTS AND DISCUSSION

A scheme of the complete manufacturing process is displayed in Figure 1. First step consists of the composite resin formulation, then followed by the Li-ion and Na-ion battery electrodes

fabrication by means of VPP 3D printing, and additional thermal post-processing. Serving respectively as the active materials for the negative electrode and conductive additives, both commercial anatase TiO_2 and black carbon loadings were increased as high as possible (while keeping the TiO_2 :C 12:1 weight ratio) in the polymeric resin. This was achieved to enhance the electrochemical performances of the printed electrodes and reduce the shrinkage of the electrodes upon thermal post-processing. While the classical polymer resin (composed of monomers, oligomers and a photoinitiator) greatly contributes to the printability and mechanical strength of the printed electrodes (green state), the polymer is inactive electrochemically. Thus, the polymer percentage within the composite resin must be minimized. However, the polymer must be sufficient to allow for fabrication and to lock in the intended geometry of the component. In this work, a highly loaded composite photocurable resin with composition of TiO_2 :C:Polymer 18:1.5:80.5 wt.%, specifically designed to print negative electrodes for sodium-ion and lithium-ion batteries, is presented.

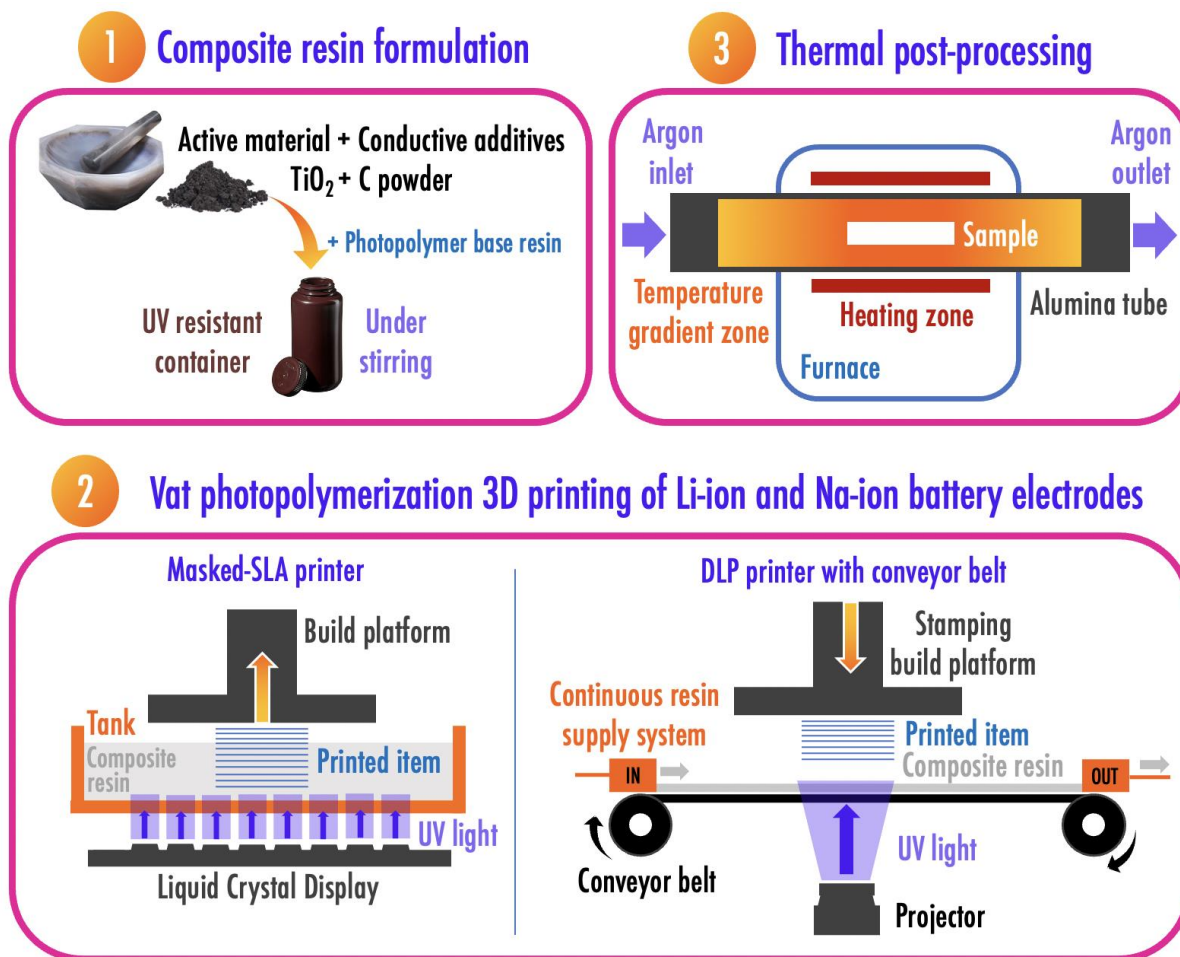


Figure 1. Scheme of the electrode manufacturing process.

Preliminary printing tests of the composite resin were performed using a classical masked SLA printer (Figure 1), equipped with a 200 cm³ capacity vat to store the photocurable resin. The introduction of a high loading of charges (active material + conductive additive) was here shown to have a detrimental effect on the printability, as particle sedimentation at the bottom of the tank led to obstruction of the recoating process, as already reported by Tan et al.²⁵. To avoid this issue, a tedious optimization process regarding the resin viscosity is often required. The introduction of smaller filler particles²⁶, viscosifier, dispersant and/or diluent²⁷ have been considered in the past.

Optical properties also need to be studied carefully as filler particles contribute to light scattering, thus having a detrimental effect on the curing depth upon printing.

To ensure a higher printing resolution of the parts, an unconventional DLP 3D printer equipped with a conveyor belt (Figure 1) allowing continuous supply of a thin layer of the composite resin (70 μm) through tape casting was instead employed. Layer after layer, the build platform moves down along the Z-axis and is pressed into the resin. The latter is selectively cured while being exposed to UV light. The unused slurry is immediately collected by a wiper and pumped back into the initial reservoir, minimizing sample waste. A new piece of foil is employed for each layer so scratches from previous layers are avoided. As the resin is continuously circulating through the pump system, the sedimentation phenomenon is eliminated, thus facilitating the printing process of highly loaded composite resins. Using this method, a solid design 3D printed electrode disc with 100% infill, serving here as reference, was obtained (Figure 2a). TGA of the 3D printed disc (green state item) under oxygen (Figure 3a) was used to verify that the amount of TiO_2 in this sample is 18 wt%. This observation confirms that the DLP 3D printer equipped with a conveyor belt allows a continuous circulation of the resin upon printing, and leads to homogeneous samples with the desired composition ($\text{TiO}_2\text{:C:Polymer}$ 18:1.5:80.5 wt.%). Such a printer design is thus particularly suitable to print battery electrodes using highly-loaded composite resins as material feedstock. Sample homogeneity was also confirmed from the SEM images (Figure 2c), in which TiO_2 particles appear well dispersed into the polymer matrix.

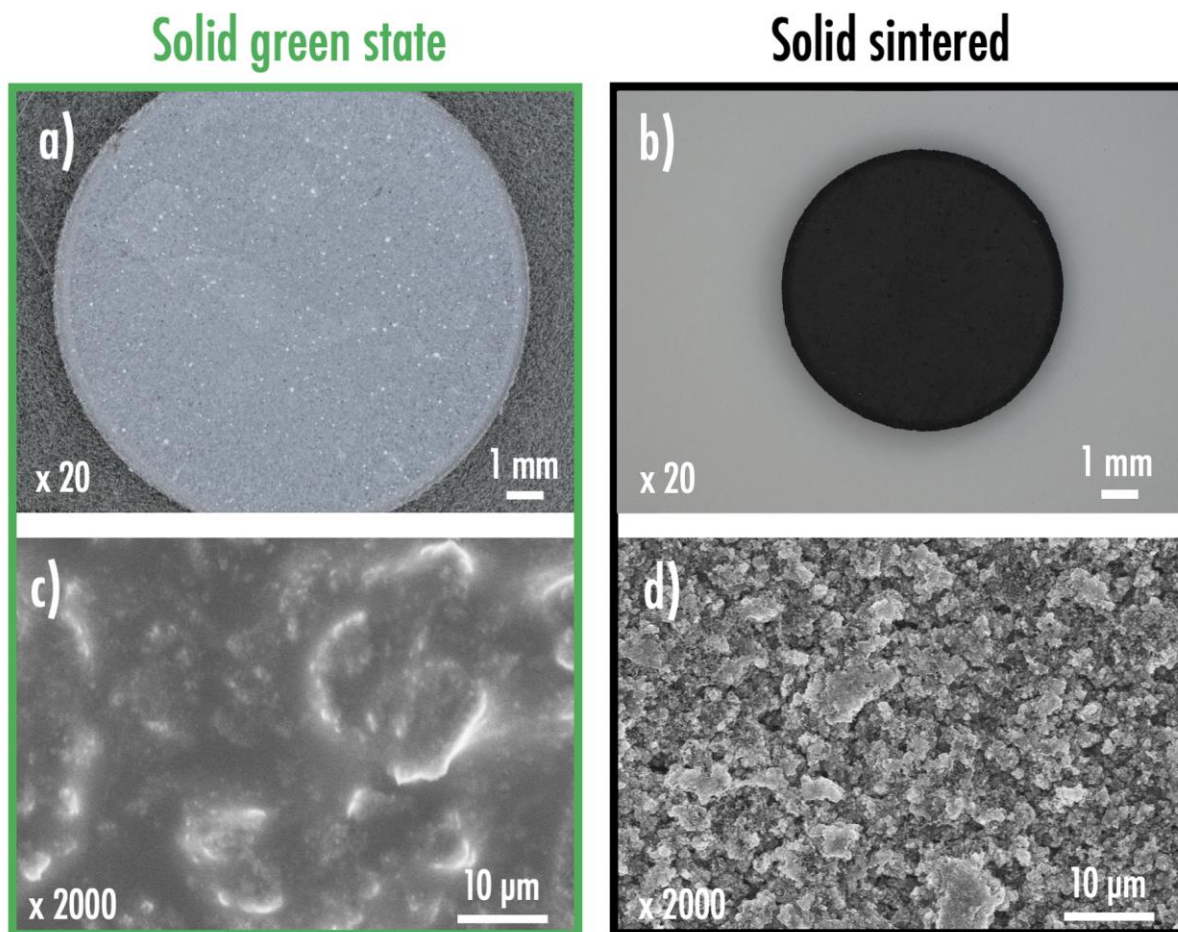


Figure 2. Optical images (a, b) and SEM micrographs (c, d) of the solid 3D printed negative electrode at the green state (green, left), and after sintering (black, right).

At this stage, the printed electrodes in the green state still contain 80.5 wt.% of electrochemically-inactive polymer, and lack porosity. Thus, to further enhance the electrochemical performances of the printed electrode, a thermal post-processing step with a profile including debinding to allow polymer removal was implemented. Figure 2b shows the electrode after the sintering process where a well defined part without distortion or cracks is observed. A SEM micrograph (Figure 2d) clearly shows the removal of the polymeric matrix as well as the partial fusion of the TiO_2 particles. The analysis of TGA data from a 3D printed sample

of pure photopolymer base resin under an inert atmosphere showed the degradation of the polymer matrix to initiate around 150 °C with DTG peaks appearing at 340 °C and 445 °C (Figure 3b). After 500 °C, the sample almost totally decomposed with only 3 wt.% remaining corresponding to residual carbon. From these results, a debinding step was set between room temperature and 500 °C to limit the crack formation upon polymer sublimation, followed by a sintering step up to 700 °C to ensure adequate mechanical strength of the electrode and to allow TiO₂ particles fusing (Figure 3c). After the thermal post-processing, the sintered electrodes presented a homogenous microporosity created by the polymer removal (Figure 2d), and a shrinkage of 42% along the X and Y axis and 38% along the Z axis was measured. Through XRD analysis it was confirmed that the initial TiO₂ anatase tetragonal symmetry in the I41/amd space group was maintained after the sintering process, meaning that the crystallographic structure was not affected by the maximum temperature of 700 °C (Figure 3d).

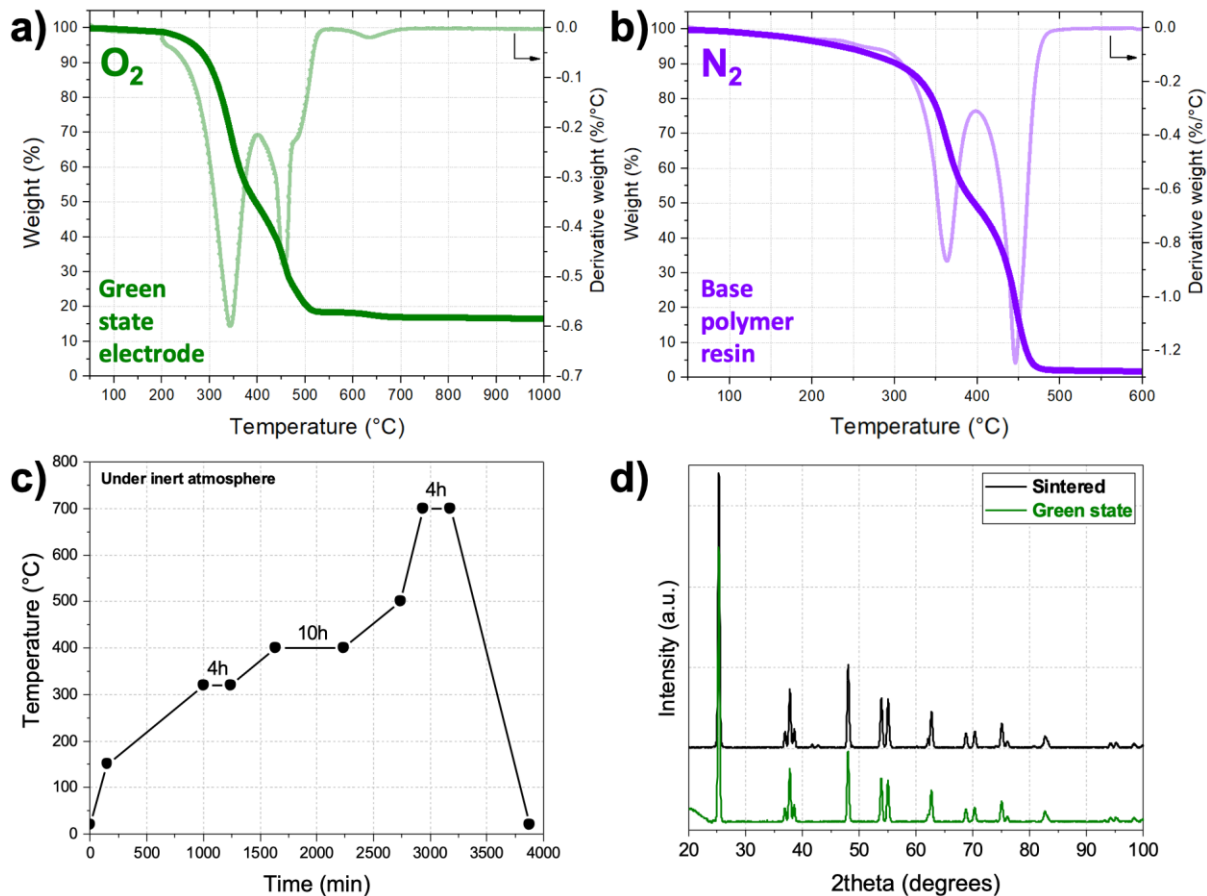


Figure 3. TGA-DTG analysis of (a) a green state 3D printed electrode analyzed in O₂, and of (b) the base polymeric resin analyzed in N₂; (c) Thermal profile for the debinding and sintering of the 3D printed negative electrodes. (d) Comparison of XRD diffractograms from sintered and green state 3D printed electrodes.

Appearing as an important parameter for the correct function of battery electrodes, the relatively low electronic conductivity (ca. $10^{-12} - 10^{-7} \text{ S.cm}^{-1}$ ²⁸) of TiO₂ was partially compensated in this work by adding nanosized conductive carbon particles. The electronic conductivity of the sintered electrode was measured to be 3.5 mS.cm^{-1} , a great improvement when comparing against the green state counterpart that was totally insulator, that can be here simply explained by the creation of an electronic percolation network between TiO₂ and conductive carbon nanoparticles after the removal of the insulator polymer matrix. Moreover, the aforementioned 3 wt.% of residual carbon

that originated from the pyrolysis of the polymer matrix might contribute to the improved conductivity, but its contribution is uncertain at this point.

The electrochemical performances of the solid green state and sintered electrodes were investigated in sodium-ion battery half cell configuration at current densities of $1 \text{ mA.g}^{-1}_{\text{TiO}_2}$ and $5 \text{ mA.g}^{-1}_{\text{TiO}_2}$ (Figure S.1). Due to the lack of micro-porosity and isolated TiO_2/C particles within the polymer matrix, in addition to the consequent inability of Na^+ to intercalate, the green state electrode behavior depicts insignificant specific capacity values. The sintered sample exhibits slightly greater electrochemical response due to the higher electronic conductivity and improved porosity leading to enhanced liquid electrolyte impregnation. Nevertheless, the solid sintered electrode depicts low initial discharge specific capacity of only 2 mAh.g^{-1} at $1 \text{ mA.g}^{-1}_{\text{TiO}_2}$, and a consecutive gradual increase over the cycles (6 mAh.g^{-1} is reached after 5 cycles). The relatively low capacity values obtained here for this solid sintered electrode disc can be explained by the 100% infill density 3D architecture that heavily hinders the electrolyte impregnation along the entire thickness of the electrode ($550 \text{ }\mu\text{m}$), as already witnessed in literature for 3D printed electrodes¹⁸. The slow electrolyte impregnation phenomenon can be identified as the continuous increase of specific discharge capacity upon cycling, even after having applied an initial resting time of 20 hours. Most of the electrolyte remains only on the surface thus preventing all the active material particles from reacting electrochemically.

In order to further enhance the electrochemical performances of the sintered electrode and address the aforementioned electrolyte impregnation issue while also maintaining enough mechanical strength for adequate handling, two other electrode discs with different infill patterns (Figure 4) have been specially designed, 3D printed, and subjected to thermal post-processing. The first design consisted in a gyroid-type infill pattern (Figure 4a) with a 50% density and the second

in a cubic pattern (Figure 4b) with an infill density of 78%. The electronic conductivity of these sintered electrodes was increased when an infill pattern was incorporated. The gyroid sintered electrode (Figure 4c) led to the greatest conductivity with 12.8 mS.cm^{-1} , while the cubic sintered sample (Figure 4d) exhibited 5.8 mS.cm^{-1} , and the solid sintered electrode (Figure 2b) 3.5 mS.cm^{-1} . This trend might be explained by an improved accommodation of the solid charges occurring during debinding and sintering, facilitated by the infill macroporosity channels presence, thus ultimately leading to an improved electronic percolation network. When observed by SEM, the microporosity of the sintered electrodes remain unchanged (Figure 4e and 4f), regardless of the incorporation of an infill/macroporosity pattern, even when compared to the solid sample with 100% infill density (Figure 2d).

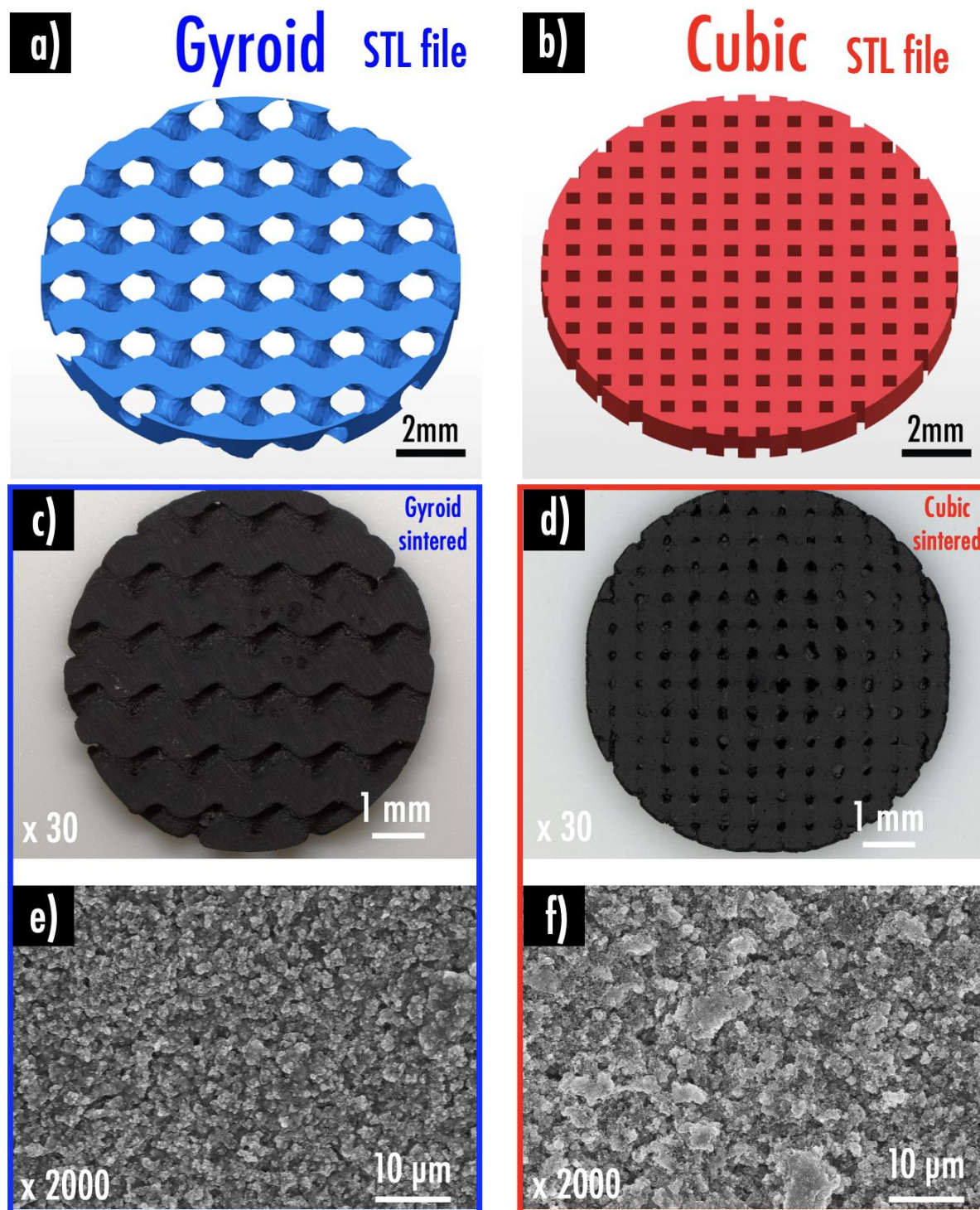


Figure 4. CAD-files of the (a) gyroid and (b) cubic electrode discs; Optical images (c, d) and SEM micrographs (e, f) of the gyroid sintered (blue, left) and cubic sintered (red, right) 3D negative electrode discs.

Flexural tests were then performed on the printed electrodes. From these tests, it was observed that the solid sintered electrode displayed a superior mechanical performance when compared with the green state counterpart (Table 1). The solid sintered electrode yielded a specific flexural strength about 8% higher than that shown by the green state sample, still containing the polymeric matrix. These results can be explained by the fusion of the ceramic particles during the sintering stage (Figure S.2) as reported by Mummareddy et al.²⁹. When comparing the stress-strain profiles of the solid electrodes in the green and sintered state (Figure 5a), it can be observed that the green sample exhibits a relatively higher ductility than the sintered specimen due the influence of the polymer resin. In contrast, the solid sintered sample exhibits a clear brittle behavior, with a short plateau at about 23 MPa probably caused by the interlayer delamination/propagation process observed on the samples, a well known mechanism associated with the energy release rate during delamination³⁰. The mechanical properties of the printed electrodes compare well with the measurements reported by Zhu et al.³¹ in electrodes produced through the traditional tape casting method (a numeric comparison is not given since different variables interfere). The sintered solid electrode displays a modulus of 3.41 GPa, which is about 6.5 times stiffer when compared to its green counterpart (0.52 GPa) that still contains the polymer resin, making it comparatively more rigid.

As expected from the mechanical standpoint, the introduction of gyroid and cubic lattice patterns reduce the mechanical performances of the sintered electrodes when compared to the solid sample with 100% infill density. Indeed, as displayed in Table 1, the flexural strength of the sintered gyroid and cubic electrodes is respectively 43% and 20% lower than what was observed for the sintered solid electrode. The sintered cubic sample is the stiffest of all the configurations with a flexural modulus value of 4.03 GPa while the sintered gyroid electrode has a lower flexural

modulus of 2.22 GPa given its structural configuration, which directly impacts its rigidity under flexion. Finally, when comparing their respective specific flexural strength, it can be observed that although the solid sintered electrode is still the stronger configuration, the investigated designs all appear to be in a close range spanning between 16 and 20 MPa.cm³/g. Regarding the hardness, using a nanoindentation machine, a value of 0.035 GPa (at a maximum load of 60mN and a maximum depth of 9µm) was recorded for the sintered electrodes, a value 30% higher than what was measured for the green state sample, and in good agreement with the trend observed in literature ³².

Table 1. Mechanical properties of the solid, gyroid and cubic electrode designs specimens. Standard deviation is in parenthesis.

Sample	Flexural strength (MPa)	Flexural modulus (GPa)	Density (g/cm ³)	Specific flexural strength (MPa.cm ³ /g)
Solid green state	25.22 (3.5)	0.52 (0.02)	1.34	18.8
Solid sintered	32.8 (2.1)	3.41 (0.85)	1.61	20.4
Gyroid sintered	18.72 (6.4)	2.22 (0.46)	1.17	16.0
Cubic sintered	26.37 (5.0)	4.03 (1.1)	1.60	16.5

From the electrochemical standpoint, the gyroid and cubic infill patterns unquestionably enabled a better impregnation of the electrolyte within the sintered electrodes, consequently leading to greater specific capacities (Figure 5b). The cubic sample exhibited an initial specific discharge capacity of 122 mAh.g⁻¹ at a current density of 1 mA.g⁻¹ and an irreversible capacity loss of 63%.

In Figure 5d it can be observed that most of this capacity is obtained below 0.25 V vs. Na/Na⁺. At 1, 5 and 10 mA.g⁻¹ current densities, mean capacities of 45, 19 and 12 mAh.g⁻¹ were observed, respectively. When passing from cubic to gyroid geometry, greater specific capacities were witnessed (Figure 5b), but the individual electrochemical processes remained almost identical (Figure 5c and d). Gyroid sintered sample displayed a similar irreversible capacity of 60%, but an initial specific discharge capacity of 164 mAh.g⁻¹ at a current density of 1 mA.g⁻¹_{TiO₂}. At 1, 5 and 10 mA.g⁻¹_{TiO₂} current densities, mean capacities of 63 mAh.g⁻¹ (1.4x higher than cubic), 36 mAh.g⁻¹ (1.9x higher than cubic) and 25 mAh.g⁻¹ (2.1x higher than cubic) were observed, respectively. When returning to a slower current density of 1 mA.g⁻¹_{TiO₂}, good capacity retention was observed for both samples. The drastic improvement in specific discharge capacities when compared with the reference solid sintered electrode, whose values at every current density are insignificant, shows the impact of electrode design when manufacturing through 3D printing. These values are still far from tape-cast TiO₂ film that was reported to achieve 100 mAh.g⁻¹ at 37 mA.g⁻¹ in a similar configuration (also using NaPF₆ as electrolyte salt, but with a lower cut-off voltage of 0.02 V)¹¹. While theoretical capacity of TiO₂ based on the uptake of one Na⁺ during the Ti⁴⁺/Ti³⁺ redox reaction is 335 mAh.g⁻¹, this value has been attained only by either expensive or complicated methods to synthesize TiO₂ (this work in contrast, utilizes commercial nanosized TiO₂). These methods include crystallographically oriented nanoparticle subunits and high surface area (204 m².g⁻¹³³, 157 m².g⁻¹⁶), or hierarchical porous structures which combines macropores (1.5–2.5 μm) and mesopores (9.78 nm)³⁴, or doping methods^{35,36}. Another reason for the difficulty in attaining the theoretical value is the sluggish sodium-ion migration³⁷.

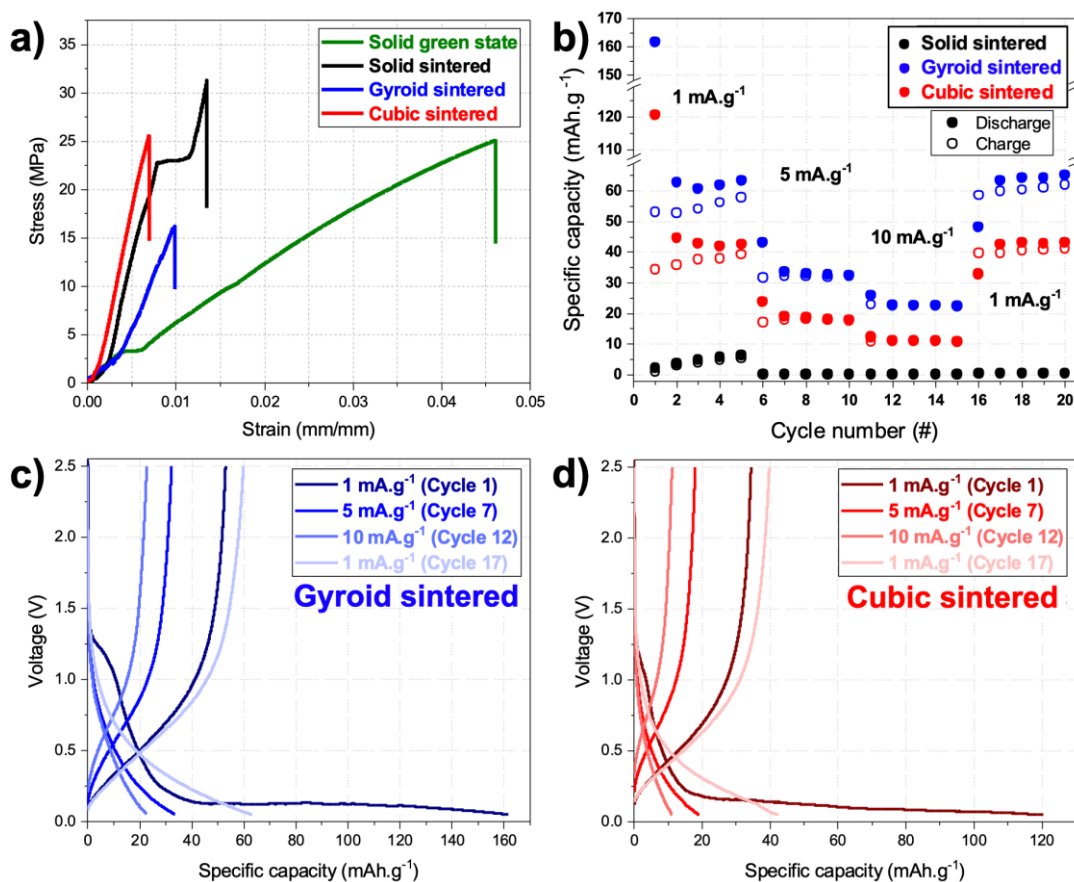


Figure 5. (a) Stress-Strain curves of the 3D electrode specimens; (b) Rate capability tests in half-cell configuration of the 3D printed structures versus sodium metal; Charge/discharge capacity profiles for the (c) gyroid sintered and (d) cubic sintered samples versus sodium metal.

As the best electrochemical results in sodium-ion configuration were obtained with the gyroid 3D design, it was also tested as a negative electrode versus lithium metal in half-cell configuration (Figure 6a and b). Initially, the gyroid sintered sample displayed an initial specific discharge capacity of 371 mAh.g⁻¹ at a current density of 1 mA.g⁻¹_{TiO₂}, very close to the capacity delivered by commercial graphite³⁸. However, this value decreased rapidly in the second cycle to 140 mAh.g⁻¹ accompanied by an irreversible capacity loss of 62%. This capacity fade is comparable to the loss observed when cycling a similar electrode versus sodium. In both cases, this is in part due

to the loss of exchangeable sodium or lithium ions as a result of the inadequate formation of a solid electrolyte interphase (SEI) layer and to the chemical and electrochemical parasitic reactions that may occur with residual carbon-based compounds (not necessarily conductive) left from the sintering process. Nonetheless, from Figure 6b it can be observed that for lithium (and also sodium in Figure 5c) it seems that the main capacity loss is related to the absence of the processes occurring below 0.5 V vs. Li/Li⁺ (or Na/Na⁺). This process is probably associated with lithium and sodium plating. After 5 cycles at 1 mA.g⁻¹_{TiO₂}, the capacity stabilized around 113 mAh.g⁻¹, while the specific capacity decreased to values around 30 mAh.g⁻¹ at a current density of 5 mA.g⁻¹_{TiO₂}. The clear plateau at around 2.0 V observed during the charge process in cycles 1, 2 and 6 (Figure 6b) is characteristic for lithium-ion deintercalation reaction into an anatase lattice ³⁹.

These results demonstrate that for a gyroid sintered electrode, at low current densities more capacity is obtained from the intercalation and deintercalation of lithium in comparison with sodium. However, the contrary is observed at a higher current density, when the capacity obtained from sodium intercalation exceeds that from lithium. In terms of the materials, for both lithium and sodium storage the problem of low capacity could be overcome by decreasing the particle size or increasing the specific surface area of anatase TiO₂ by utilizing highly mesoporous structures and nano-sized particles and by combining this strategy with a carbon coating strategy to improve the electronic conductivity ⁴⁰.

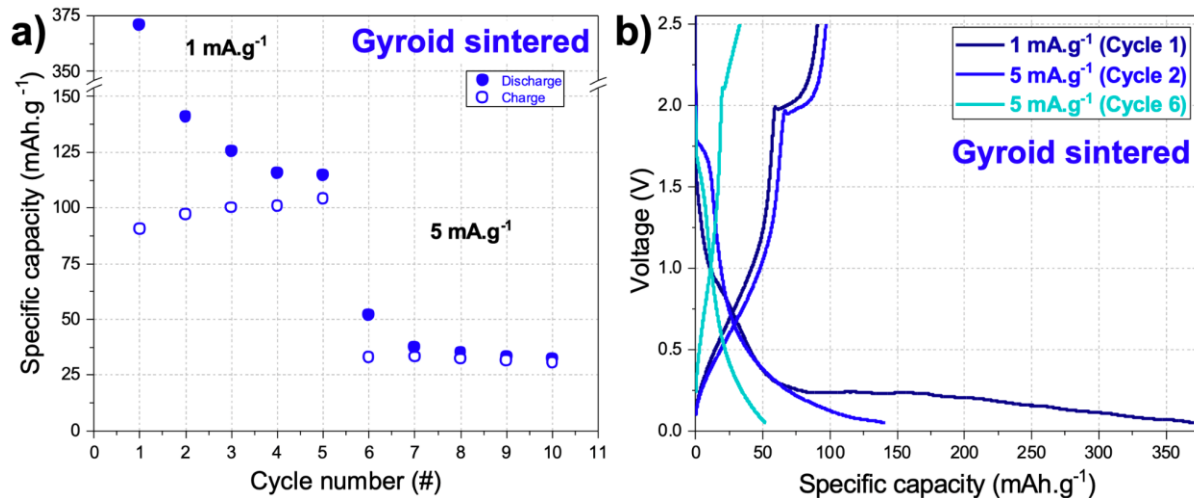


Figure 6. (a) Rate capability tests in half-cell configuration of the gyroid sintered electrode versus lithium metal; (b) Charge/discharge capacity profiles for the gyroid sintered tested versus lithium metal.

Finally, a simulation study was accomplished by finite-element method software (Comsol Multiphysics) (Figure 7), in order to better understand the Li⁺ distribution profiles within the solid sintered and gyroid sintered electrodes during discharge (when tested in a half-cell configuration *versus* lithium metal). In good agreement with the observations from literature ^{41,42}, at t=0, the TiO₂ electrodes are fully delithiated (Figure 7a and 7e), while the Li⁺ ions diffuse during discharge (lithiation step) from the Li metal to the 3D printed TiO₂ electrode over time. The solid sintered planar electrode configuration (Figure 7a-d) is thick (550 μm) and lacks porosity. In this context, the Li⁺ ions being intercalated upon discharge are not able to entirely go through the thickness, thus creating a depletion zone at the electrode side facing the current collector. This phenomenon can be explained by the longer distance that these Li⁺ ions need to travel. On the contrary, upon discharge, a Li⁺-rich zone (higher Li⁺ concentration) appears near the separator/electrolyte (the closest to the Li metal electrode) as Li⁺ need to travel a shorter distance. These gradients are

attenuated due to the introduction of the gyroid design. Indeed, the gyroid sintered electrode configuration (Figure 7e-h) presents a macroporosity pattern that contributes to an improved Li^+ distribution within the electrode thickness during discharge.

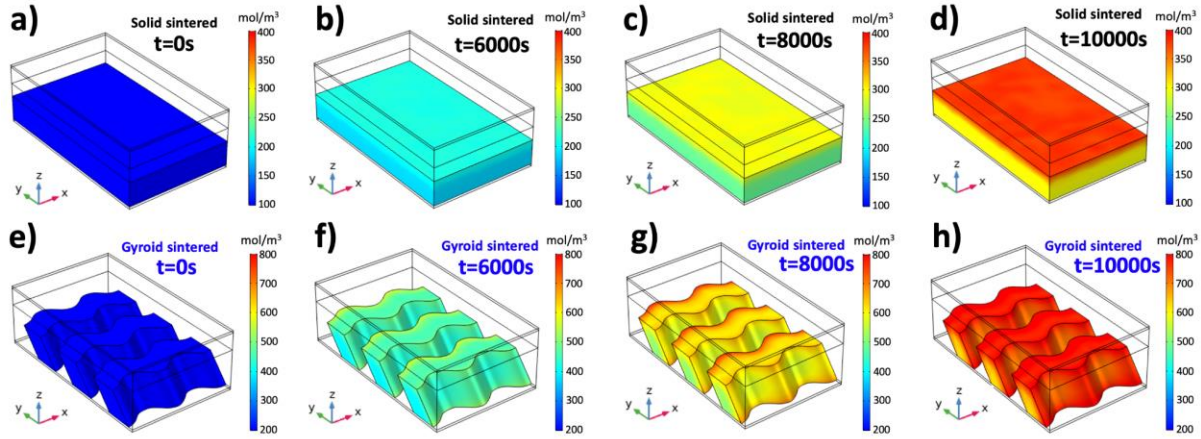


Figure 7. Li^+ concentration within the 3D printed electrodes (solid sintered=top; and gyroid sintered=bottom) during the discharge step at (a and e) $t=0\text{s}$; (b and f) $t=6000\text{s}$; (c and g) $t=8000\text{s}$; and (d and h) $t=10000\text{s}$. Simulation parameters employed for this study are summarized in Table S.1.

4. CONCLUSIONS

For the first time, a vat photopolymerization 3D printable TiO_2 -loaded composite photocurable resin has been specifically developed to manufacture sodium-ion and lithium-ion battery negative electrodes. Loadings of active material and conductive additives in the composite photocurable resin were increased as high as possible to enhance the electrochemical performances of the printed electrode. In order to facilitate the printability of electrodes from such highly-loaded composite resin, the authors suggest to use a VPP printer equipped with a conveyor belt allowing continuous supply of a homogeneous thin layer of the composite resin. When tested in sodium-ion battery half

cell configuration, the 3D printed electrodes (green state) discs with 100% infill pattern depicted very poor reversible specific capacity due to the lack of macro and micro-porosity. Electroactive species were shown to be completely immersed within the polymer matrix. The introduction of an additional debinding post-processing step allowed the removal of the electrochemically inactive polymer matrix, thus creating a micro-porosity leading to greater electrochemical performances upon cycling, but at the expense of the ductility. A compromise between electrochemical and mechanical properties must be reached. The incorporation of a gyroid or cubic infill pattern (macroporosity) within the electrode during printing was shown to improve the liquid electrolyte impregnation and final reversible specific capacities upon cycling of the sintered electrodes, while decreasing the flexural strength. Gyroid pattern exhibited the greatest electronic conductivity (12.8 mS.cm^{-1}) and discharge specific capacities (63 mAh.g^{-1} , 36 mAh.g^{-1} and 25 mAh.g^{-1} at 1, 5 and 10 mA.g^{-1} current densities, respectively) in sodium-ion battery half cell configuration. When tested in lithium-ion battery half cell configuration *versus* lithium metal, the sintered gyroid electrode displayed discharge specific capacities of 113 mAh.g^{-1} after 5 cycles at 1 mA.g^{-1} , and 30 mAh.g^{-1} at 5 mA.g^{-1} , thus confirming that these 3D printed TiO_2 -based electrodes can serve as negative electrodes in both sodium-ion and lithium-ion configuration after enduring a thermal post-processing step. The presence of a Li^+ concentration gradient within the sintered electrodes during discharge was highlighted thanks to a simulation study. Through the introduction of the gyroid electrode design, the associated macroporosity was shown to contribute to an improved Li^+ distribution.

These first results set the foundation for the development of intricate 3D printed electrodes. To further enhance the electrochemical properties, future studies must be focused on the optimization of the particle size so that the ion diffusion distance is shortened, and on the development of an

electronically conductive coating on top of the active particles that could lead to improved rate capability. From the printing aspect, future works must now be focused on the development and 3D printing of additional composite resins corresponding to each component of a classical battery (positive electrode, current collectors, separator, electrolyte). Using a multi-material VPP 3D printing option ^{43,44}, the printability of a complete sodium-ion or lithium-ion battery in one single process could be envisioned. Research must also be devoted to technically improving multi-material 3D printer resolution and software to manufacture intricate 3D battery architectures. This work is the first step towards the development of shape-conformable batteries allowing for optimization of energy storage for a final end-use application by leveraging unused dead-volume.

ASSOCIATED CONTENT

Supporting information.

Rate capability tests in half-cell configuration of sintered and green state 3D printed solid negative electrodes versus sodium metal; SEM micrographs of bare TiO₂ powder and a gyroid sintered electrode with visible TiO₂ particles fused together; Simulation parameters employed in COMSOL multiphysics 5.4 lithium-ion battery module software (PDF).

AUTHOR INFORMATION

Corresponding Authors

Alexis Maurel – Department of Aerospace and Mechanical Engineering, The University of Texas at El Paso, El Paso, TX 79968, USA; Email: amaurel@utep.edu

Pedro Cortes – Materials Science and Engineering Department, Youngstown State University, Youngstown, OH 44555, USA; Email: pcortes@ysu.edu

ACKNOWLEDGMENTS

This work was supported by the French Fulbright Program, the NASA Space Mission Directorate's Early Career Initiative Program, the Friedman endowment chair at Youngstown State University, and the University of Texas at El Paso (UTEP) Murchison Chair.

REFERENCES

- (1) Maurel, A.; Martinez, A. C.; Dornbusch, D. A.; Huddleston, W. H.; Seol, M.-L.; Henry, C. R.; Jones, J. M.; Yelamanchi, B.; Bakhtar Chavari, S.; Edmunson, J. E.; Sreenivasan, S. T.; Cortes, P.; MacDonald, E.; Sherrard, C. G. What Would Battery Manufacturing Look Like on the Moon and Mars? *ACS Energy Lett.* **2023**, 1042–1049.
- (2) Madian, M.; Eychmüller, A.; Giebeler, L. Current Advances in TiO₂-Based Nanostructure Electrodes for High Performance Lithium Ion Batteries. *Batteries* **2018**, 4 (1), 7.
- (3) Wang, W.; Liu, Y.; Wu, X.; Wang, J.; Fu, L.; Zhu, Y.; Wu, Y.; Liu, X. Advances of TiO₂ as Negative Electrode Materials for Sodium-Ion Batteries. *Adv. Mater. Technol.* **2018**, 3 (9), 1800004.
- (4) Liu, H.; Bi, Z.; Sun, X.-G.; Unocic, R. R.; Paranthaman, M. P.; Dai, S.; Brown, G. M. Mesoporous TiO₂-B Microspheres with Superior Rate Performance for Lithium Ion Batteries. *Adv. Mater.* **2011**, 23 (30), 3450–3454.
- (5) Ren, Y.; Liu, Z.; Pourpoint, F.; Armstrong, A. R.; Grey, C. P.; Bruce, P. G. Nanoparticulate TiO₂(B): An Anode for Lithium-Ion Batteries. *Angew. Chem. Weinheim Bergstr. Ger.* **2012**, 124 (9), 2206–2209.

- (6) Hong, Z.; Zhou, K.; Zhang, J.; Huang, Z.; Wei, M. Facile Synthesis of Rutile TiO₂ Mesocrystals with Enhanced Sodium Storage Properties. *J. Mater. Chem. A Mater. Energy Sustain.* **2015**, 3 (33), 17412–17416.
- (7) Hong, Z.; Hong, J.; Xie, C.; Huang, Z.; Wei, M. Hierarchical Rutile TiO₂ with Mesocrystalline Structure for Li-Ion and Na-Ion Storage. *Electrochim. Acta* **2016**, 202, 203–208.
- (8) He, H.; Wang, H.; Sun, D.; Shao, M.; Huang, X.; Tang, Y. N-Doped Rutile TiO₂/C with Significantly Enhanced Na Storage Capacity for Na-Ion Batteries. *Electrochim. Acta* **2017**, 236, 43–52.
- (9) González, J. R.; Alcántara, R.; Nacimiento, F.; Ortiz, G. F.; Tirado, J. L. Microstructure of the Epitaxial Film of Anatase Nanotubes Obtained at High Voltage and the Mechanism of Its Electrochemical Reaction with Sodium. *CrystEngComm* **2014**, 16 (21), 4602–4609.
- (10) Oh, S.-M.; Hwang, J.-Y.; Yoon, C. S.; Lu, J.; Amine, K.; Belharouak, I.; Sun, Y.-K. High Electrochemical Performances of Microsphere C-TiO₂ Anode for Sodium-Ion Battery. *ACS Appl. Mater. Interfaces* **2014**, 6 (14), 11295–11301.
- (11) Wu, L.; Buchholz, D.; Bresser, D.; Gomes Chagas, L.; Passerini, S. Anatase TiO₂ Nanoparticles for High Power Sodium-Ion Anodes. *J. Power Sources* **2014**, 251, 379–385.
- (12) Su, D.; Dou, S.; Wang, G. Anatase TiO₂: Better Anode Material Than Amorphous and Rutile Phases of TiO₂ for Na-Ion Batteries. *Chem. Mater.* **2015**, 27 (17), 6022–6029.
- (13) Long, J. W.; Dunn, B.; Rolison, D. R.; White, H. S. Three-Dimensional Battery Architectures. *Chem. Rev.* **2004**, 104 (10), 4463–4492.

- (14) Maurel, A.; Courty, M.; Fleutot, B.; Tortajada, H.; Prashantha, K.; Armand, M.; Grugeon, S.; Panier, S.; Dupont, L. Highly Loaded Graphite–Polylactic Acid Composite-Based Filaments for Lithium-Ion Battery Three-Dimensional Printing. *Chem. Mater.* **2018**, *30* (21), 7484–7493.
- (15) Maurel, A.; Grugeon, S.; Fleutot, B.; Courty, M.; Prashantha, K.; Tortajada, H.; Armand, M.; Panier, S.; Dupont, L. Three-Dimensional Printing of a LiFePO₄/Graphite Battery Cell via Fused Deposition Modeling. *Sci. Rep.* **2019**, *9* (1), 18031.
- (16) Maurel, A.; Armand, M.; Grugeon, S.; Fleutot, B.; Davoisne, C.; Tortajada, H.; Courty, M.; Panier, S.; Dupont, L. Poly(Ethylene Oxide)–LiTFSI Solid Polymer Electrolyte Filaments for Fused Deposition Modeling Three-Dimensional Printing. *J. Electrochem. Soc.* **2020**, *167* (7), 070536.
- (17) Martinez Maciel, A. C.; Maurel, A.; Sreenivasan, S. T.; MacDonald, E. 3D Printing of Lithium-Ion Battery Components Via Vat Photopolymerization. *Meet. Abstr.* **2021**, *MA2021-02* (1), 55.
- (18) Maurel, A.; Russo, R.; Grugeon, S.; Panier, S.; Dupont, L. Environmentally Friendly Lithium-Terephthalate/Polylactic Acid Composite Filament Formulation for Lithium-Ion Battery 3D-Printing via Fused Deposition Modeling. *ECS J. Solid State Sci. Technol.* **2021**, *10* (3), 037004.
- (19) Maurel, A.; Kim, H.; Russo, R.; Grugeon, S.; Armand, M.; Panier, S.; Dupont, L. Ag-Coated Cu/polylactic Acid Composite Filament for Lithium and Sodium-Ion Battery Current Collector Three-Dimensional Printing via Thermoplastic Material Extrusion. *Front. Energy Res.* **2021**, *9*. <https://doi.org/10.3389/fenrg.2021.651041>.

- (20) Martinez, A. C.; Maurel, A.; Aranzola, A. P.; Grugeon, S.; Panier, S.; Dupont, L.; Hernandez-Viezcas, J. A.; Mummareddy, B.; Armstrong, B. L.; Cortes, P.; Sreenivasan, S. T.; MacDonald, E. Additive Manufacturing of $\text{LiNi}_{1/3}\text{Mn}_{1/3}\text{Co}_{1/3}\text{O}_2$ Battery Electrode Material via Vat Photopolymerization Precursor Approach. *Sci. Rep.* **2022**, *12* (1), 19010.
- (21) Narita, K.; Saccone, M. A.; Sun, Y.; Greer, J. R. Additive Manufacturing of 3D Batteries: A Perspective. *J. Mater. Res.* **2022**, *37* (9), 1535–1546.
- (22) Maurel, A.; Grugeon, S.; Armand, M.; Fleutot, B.; Courty, M.; Prashantha, K.; Davoisne, C.; Tortajada, H.; Panier, S.; Dupont, L. Overview on Lithium-Ion Battery 3D-Printing By Means of Material Extrusion. *ECS Trans.* **2020**, *98* (13), 3.
- (23) Maurel, A.; Martinez, A. C.; Grugeon, S.; Panier, S.; Dupont, L.; Cortes, P.; Sherrard, C. G.; Small, I.; Sreenivasan, S. T.; Macdonald, E. Toward High Resolution 3D Printing of Shape-Conformable Batteries via Vat Photopolymerization: Review and Perspective. *IEEE Access* **2021**, *9*, 140654–140666.
- (24) Manogharan, G.; Yelamanchi, B.; Aman, R.; Mahbooba, Z. Experimental Study of Disruption of Columnar Grains During Rapid Solidification in Additive Manufacturing. *JOM* **2016**, *68* (3), 842–849.
- (25) Tan, L. J.; Zhu, W.; Zhou, K. Recent Progress on Polymer Materials for Additive Manufacturing. *Adv. Funct. Mater.* **2020**, *30* (43), 2003062.
- (26) Yugang, D.; Yuan, Z.; Yiping, T.; Dichen, L. Nano- TiO_2 -modified Photosensitive Resin for RP. *Rapid Prototyping Journal* **2011**, *17* (4), 247–252.

- (27) Hinczewski, C.; Corbel, S.; Chartier, T. Ceramic Suspensions Suitable for Stereolithography. *J. Eur. Ceram. Soc.* **1998**, *18* (6), 583–590.
- (28) Du, X.; Wang, Q.; Feng, T.; Chen, X.; Li, L.; Li, L.; Meng, X.; Xiong, L.; Sun, X.; Lu, L.; Xu, Y. One-Step Preparation of Nanoarchitected TiO₂ on Porous Al as Integrated Anode for High-Performance Lithium-Ion Batteries. *Sci. Rep.* **2016**, *6*, 20138.
- (29) Mummareddy, B.; Maravola, M.; MacDonald, E.; Walker, J.; Hetzel, B.; Conner, B.; Cortes, P. The Fracture Properties of Metal-ceramic Composites Manufactured via Stereolithography. *Int. J. Appl. Ceram. Technol.* **2020**, *17* (2), 413–423.
- (30) François, D.; Pineau, A.; Zaoui, A. Fracture Mechanics. In *Mechanical Behaviour of Materials: Volume II: Fracture Mechanics and Damage*; François, D., Pineau, A., Zaoui, A., Eds.; Springer Netherlands: Dordrecht, 2013; pp 7–102.
- (31) Zhu, J.; Zhang, X.; Sahraei, E.; Wierzbicki, T. Deformation and Failure Mechanisms of 18650 Battery Cells under Axial Compression. *J. Power Sources* **2016**, *336*, 332–340.
- (32) Owen, D.; Hickey, J.; Cusson, A.; Ayeni, O. I.; Rhoades, J.; Deng, Y.; Zhang, Y.; Wu, L.; Park, H.-Y.; Hawaldar, N.; Raikar, P. P.; Jung, Y.-G.; Zhang, J. 3D Printing of Ceramic Components Using a Customized 3D Ceramic Printer. *Progress in Additive Manufacturing* **2018**, *3* (1), 3–9.
- (33) Hong, Z.; Zhou, K.; Huang, Z.; Wei, M. Iso-Oriented Anatase TiO₂ Mesocages as a High Performance Anode Material for Sodium-Ion Storage. *Sci. Rep.* **2015**, *5*, 11960.

- (34) Li, Y.-N.; Su, J.; Lv, X.-Y.; Long, Y.-F.; Wen, Y.-X. Yeast Bio-Template Synthesis of Porous Anatase TiO₂ and Potential Application as an Anode for Sodium-Ion Batteries. *Electrochim. Acta* **2015**, *182*, 596–603.
- (35) Usui, H.; Yoshioka, S.; Wasada, K.; Shimizu, M.; Sakaguchi, H. Nb-Doped Rutile TiO₂: A Potential Anode Material for Na-Ion Battery. *ACS Appl. Mater. Interfaces* **2015**, *7* (12), 6567–6573.
- (36) Usui, H.; Domi, Y.; Takama, K.; Tanaka, Y.; Sakaguchi, H. Tantalum-Doped Titanium Oxide with Rutile Structure as a Novel Anode Material for Sodium-Ion Battery. *ACS Appl. Energy Mater.* **2019**, *2* (5), 3056–3060.
- (37) Li, M.; Du, Z.; Khaleel, M. A.; Belharouak, I. Materials and Engineering Endeavors towards Practical Sodium-Ion Batteries. *Energy Storage Materials* **2020**, *25*, 520–536.
- (38) Asenbauer, J.; Eisenmann, T.; Kuenzel, M.; Kazzazi, A.; Chen, Z.; Bresser, D. The Success Story of Graphite as a Lithium-Ion Anode Material – Fundamentals, Remaining Challenges, and Recent Developments Including Silicon (oxide) Composites. *Sustainable Energy Fuels* **2020**, *4* (11), 5387–5416.
- (39) Wu, F.; Li, X.; Wang, Z.; Guo, H.; Wu, L.; Xiong, X.; Wang, X. A Novel Method to Synthesize Anatase TiO₂ Nanowires as an Anode Material for Lithium-Ion Batteries. *J. Alloys Compd.* **2011**, *509* (8), 3711–3715.
- (40) Liu, Y.; Yang, Y. Recent Progress of TiO₂-Based Anodes for Li Ion Batteries. *J. Nanomater.* **2016**, *2016*. <https://doi.org/10.1155/2016/8123652>.

- (41) Dai, M.; Huo, C.; Zhang, Q.; Khan, K.; Zhang, X.; Shen, C. Electrochemical Mechanism and Structure Simulation of 2D Lithium-Ion Battery. *Adv. Theory Simul.* **2018**, *1* (10), 1800023.
- (42) Cunningham, B. *Modeling electrochemical processes in a solid-state lithium-ion battery*. COMSOL. <https://www.comsol.com/blogs/modeling-electrochemical-processes-in-a-solid-state-lithium-ion-battery/> (accessed 2023-02-06).
- (43) Choi, J. W.; Kim, H. C.; Wicker, R. Multi-Material Stereolithography. *J. Mater. Process. Technol.* **2011**, *211* (3), 318–328.
- (44) Choi, J. W.; MacDonald, E.; Wicker, R. Multi-Material Microstereolithography. *Int. J. Adv. Manuf. Technol.* **2010**, *49* (5-8), 543–551.